PHYSICAL REVIEW APPLIED **12,** 024038 (2019)

Electronic Fabry-Perot Cavity Engineered Nanoscale Thermoelectric Generators

Swarnadip Mukherjee and Bhaskaran Muralidharan*

Department of Electrical Engineering, Indian Institute of Technology Bombay, Powai, Mumbai 400076, India

(Received 22 February 2019; revised manuscript received 27 June 2019; published 19 August 2019)

In this work, we aim to design a heterostructure-based nanoscale thermoelectric generator that can maximize the waste-heat conversion efficiency at a given output power. The primary objective to be achieved for this is to realize a boxcar-shaped (band-pass) electronic transmission function [Phys. Rev. Lett. 112, 130601 (2014)]. In order to achieve that, we propose the use of an electronic analog of an optical Fabry-Perot cavity over a central resonant-tunneling structure. We further explore the optimum design possibilities by varying the geometry of the cavity wall to ensure a nearly perfect band-pass energy filtering of electrons. Based on our findings, we propose a general design guideline to realize such transmission and demonstrate that such devices can be excellent thermoelectric generators as compared to the existing proposals in terms of boosting the output power without a cost in efficiency. It is theoretically demonstrated using the nonequilibrium Green's function technique coupled with self-consistent charging effects that an enhancement in the maximum output power up to 116% can be achieved through this scheme at a 10% higher efficiency as compared to resonant-tunneling-based devices. Furthermore, an elaborate comparative study of the linear response parameters is also presented and explained in terms of the physical transport properties. This study suggests an optimal device design strategy for an improved thermoelectric generator and sets the stage for a class of thermoelectric generators facilitated via transmission line-shape engineering.

DOI: 10.1103/PhysRevApplied.12.024038

I. INTRODUCTION

Nanostructuring of thermoelectric (TE) materials has acquired unabated precedence over their bulk counterparts [1–8] in the last two decades due to their highly efficient energy harvesting capability. Over the years, research in this field was primarily focused on achieving a high thermoelectric figure of merit by means of transmission line-shape engineering [1–6], thermal conductivity reduction through interface engineering [9–11], and enhancement of power factor utilizing energy filtering effects [12–14]. The figure of merit concept typically assists in determining whether a material is a good thermoelectric or not. However, when actual device designs are considered, nonlinear transport studies [15,16] dealing with the trade-off between conversion efficiency and output power of the entire setup [5,17–23] have gained precedence.

In this context, an important work by Whitney [24,25] suggested that in a thermoelectric device setup, a boxcar-type electronic transmission function of a particular bandwidth can offer optimum trade-off by maximizing the efficiency at a given power. However, practical design guidelines of such types of devices are not well addressed. Several efforts have been made after that to realize such an electronic transmission feature by proper arrangements of tunnel-coupled quantum dots (QDs) [15,26].

A few recent studies [16,27] utilized the miniband feature of superlattice-based devices [28,29] to achieve the boxcar transmission profile. Further advancing on such ideas, recently, thermoelectric generator (TEG) setups augmented with an electronic antireflection cavity (ARC) [27,30] have been proposed using the basic thumb rule for ARC design [31]. These ideas proved to be far superior in terms of achieving excellent power-efficiency trade-off in comparison with the competing device proposals [16–18]. However, it should be noted that in the presence of charging effects, the superlattice designs [27] suffer from serious line-shape imperfections, which badly affect the power and trade-off characteristics. Moreover, the large number of constituting layers in such devices pose a serious threat to the precise epitaxial growth with the existing technology. On the other hand, the ARC-based proposal [30] produced an improved result but was never optimized for a further scope of improvements. The object of this paper is to hence propose a TEG device structure and explore its design space to provide robust design guidelines after examining and taking into consideration all the aforementioned aspects.

In this work, we consider a simple double-barrier resonant-tunneling (RT) structure embedded in an electronic Fabry-Perot (FP) cavity as shown schematically in

---

[*] bm@ee.iitb.ac.in

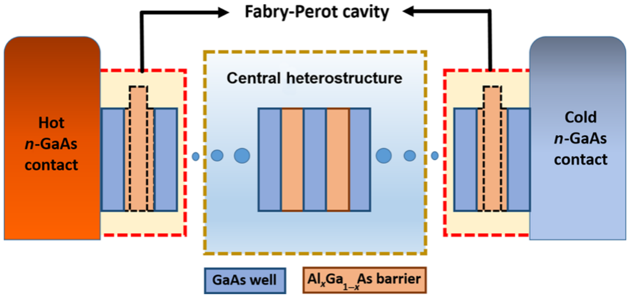

FIG. 1. Device schematic of an electronic Fabry-Perot cavity engineered heterostructure-based thermoelectric generator setup. The central region, in general, consists of a multiperiod heterostructure sandwiched between two electronic cavity sections. This work considers the use of a simple double-barrier resonant-tunneling structure embedded by cavities of varying wall geometry to optimize the desired shape of the transmission spectrum.

Fig. 1. The dotted rectangle in the cavity region denotes the variation of the width and height of the electronic potential barrier. This cavity is similar to a Fabry-Perot setup used in optics where the mirrors are replaced by rectangular tunneling electronic barriers that act as cavity walls. The transmission function, being strongly dependent on the tunneling probability through these barriers, can be tuned by varying their height and width. We show that by following a specific design guideline, a nearly band-pass transmission can be achieved by varying the wall geometry. A careful examination of the transmission function reveals that one can achieve an even wider band-pass profile compared to that of the conventional ARC-based design [30,32] by following the proposed guidelines. This setup when used as a thermoelectric generator can significantly raise the output power at a high conversion efficiency as compared to the existing proposals [5,17,27]. Exploring the design space further, it is seen that an improvement of output power up to 18% can be achieved without any degradation in the efficiency over the ARC-based structure [30].

The rest of the paper is structured as follows. In Sec. II, the variation of the transmission function with respect to the different cavity designs is thoroughly examined and explained in light of ARC physics. Based on the obtained result, three unique designs are picked for further investigation on their capability of being a good thermoelectric generator. The band schematics of all the devices are depicted in Sec. III with a clear description of their physical properties. Section IV briefly discusses the simulation setup and illustrates the formalism used. In Sec. V, the results are thoroughly discussed in terms of all the performance parameters and a detailed comparative study is presented in order to highlight the improvements achieved through the proposed design scheme. We conclude the paper in Sec. VI.

II. CAVITY PHYSICS AND TRANSMISSION FUNCTION

In this section, we closely inspect the variation of the transmission function, $T(E)$, with respect to the stoichiometric and geometric changes of the cavity wall. The thumb rule of designing an ARC says that the width (b_{FP}) and height (h_{FP}) of the rectangular cavity barriers should be exactly half and equal, respectively, to that of the central barrier region [31]. The reason behind this can be qualitatively explained in terms of the electronic Bloch states in the neighborhood of the transmission peaks of the central heterostructure [30,31,33,34]. According to the modified Kronig-Penney model, the transmission peaks of the periodic heterostructure occur when [31,35]

$$\cos(kL) = \cos\left(\frac{i\pi}{N}\right), \quad i = 1, 2, \ldots, N-1, \qquad (1)$$

where L is the length of the periodic structure; N is the number of periods; and k is the Bloch wave vector, which is defined as $k = 2\pi/\lambda$, where λ is the wavelength. Replacing k by λ in Eq. (1), we get $\lambda_i = 2L/i$, which says that twice the length of the structure should be equal to an integer multiple of the allowed wavelengths. The concept of electronic antireflection is actually borrowed from the well-known Fabry-Perot setup used in optics. To satisfy the antireflection condition, the reflected waves from the two boundaries of the cavity barrier should be exactly out of phase with each other. In other words, the cavities should act as Bragg reflectors at a wavelength λ', which satisfies the condition for thin-film interference, given by

$$2b_{\mathrm{FP}} = \left(m + \frac{1}{2}\right)\lambda', \qquad (2)$$

where λ' lies in the neighborhood of λ and m is an integer. Therefore, for $m = 0$, a unity transmission peak occurs at λ' if the cavity barriers are $\lambda'/4$ layers ($b_{\mathrm{FP}} = \lambda'/4$). This condition, along with the aforementioned relation of $L = i\lambda/2$, suggests that b_{FP} should be around half the width of the central barrier region (b) as the width of the well regions (w) throughout the structure are considered to be uniform.

In this context, one should always keep in mind that, unlike the optical setup, the height of the cavity wall plays a crucial role in tailoring the line shape of the transmission. To be more specific, the combined effect of b_{FP} and h_{FP} controls the phase of the reflected waves from the cavity wall boundaries, which in turn determines the transmission probability. By carefully examining the transmission of a setup shown in Fig. 1, we note that the amount of aberration from the band-pass nature caused by a tiny reduction in b_{FP} from $b/2$ can be compensated by a proportional upscaling of h_{FP} from h. To explain this, we draw a connection between the potential energy of the cavity barrier region (h_{FP}) and its refractive index (n). It should be noted that for a medium with refractive index n, the associated wavelength (λ_n) is defined as $\lambda_n = \lambda/n$, where λ is the corresponding vacuum wavelength. Therefore, if we replace λ' by λ'/n in Eq. (2) for $m = 0$, the condition for antireflection becomes

$$b_{\mathrm{FP}} = \frac{\lambda'}{4n}. \tag{3}$$

In the wave-particle duality picture, this wavelength is called the de Broglie wavelength of the electron, which is directly related to its momentum (p) by the relation $\lambda = h/p$. Hence, the local de Broglie wavelength of the cavity tunnel barrier can be expressed as

$$\lambda_n = \frac{\lambda}{n} = \frac{h}{\sqrt{2m(E - h_{\mathrm{FP}})}}, \tag{4}$$

where $p = \sqrt{2m(E - h_{\mathrm{FP}})}$ for a rectangular barrier of height h_{FP}, m is the effective mass of the tunnel barrier, h is the Planck's constant, E is the electron energy, and λ is the reference wavelength (here, the wavelength of the well region on both sides of the tunnel barrier). The refractive index n is thus given by Refs. [36] and [37] as

$$n = \frac{\lambda}{\lambda_n} = \sqrt{\frac{2m(E - h_{\mathrm{FP}})}{2m_0 E}}, \tag{5}$$

where the well region is having an effective mass of m_0 and zero potential energy. As we are only concerned about the energies below the cavity barrier height ($E < h_{\mathrm{FP}}$), the condition for antireflection is thus obtained by substituting the absolute value of n from Eq. (5) into Eq. (3), which is given by

$$b_{\mathrm{FP}} = \frac{\lambda'}{4}\sqrt{\frac{2m_0 E}{2m(h_{\mathrm{FP}} - E)}}. \tag{6}$$

This indicates that for the antireflection condition to prevail, any reduction in b_{FP} must be associated with a particular increase in h_{FP}. As the design energy E cannot be precisely defined, one cannot establish a specific relation between b_{FP} and h_{FP}. However, one can always predict an optimal design guideline by examining the transmission function of the RT structure embedded in an electronic FP cavity.

The above theory calls for a further investigation on the possible betterment of the boxcar nature of the transmission [30] by means of optimal cavity engineering. A quantitative measure in this regard is the transmissivity (Ω), which is the area under the flatband transmission function corresponding to the lowest transmission band, given by

$$\Omega = \int_0^{E_1} |T(E)|\, dE, \tag{7}$$

where the energy E_1 is chosen in such a way that it falls almost in between the ground and first excited band with almost zero transmission probability. The transmission function is calculated using the standard nonequilibrium Green's function (NEGF) theory [38], which is addressed later. Figure 2(a) displays the variation of Ω of the aforementioned setup as a function of b_{FP} and h_{FP} in a gray-scale color plot for a given set of RT device parameters, which is discussed in the next section. We observe that Ω exhibits a nearly hyperbolic trend around its maxima that monotonically increases (along the direction of the black dotted arrow) with decreasing b_{FP} and increasing h_{FP}. A careful investigation of the transmission reveals that its boxcar nature can almost be maintained if the percentage reduction in b_{FP} from $b/2$ is equal to half the percentage

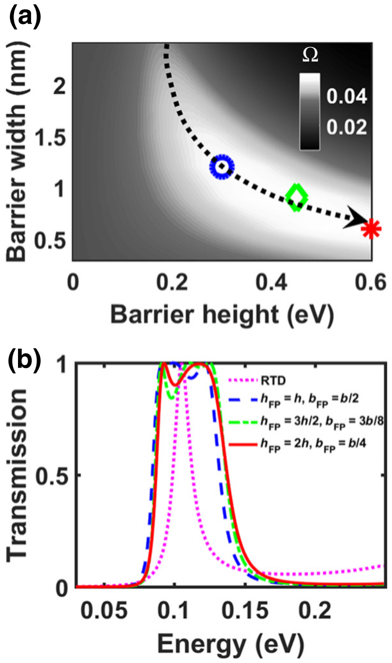

FIG. 2. Transmission function. (a) Area under the flatband transmission function corresponding to the lowest transmission band (Ω) in a gray-scale color plot as a function of the cavity wall width and height. The locus of its maxima follows a nearly hyperbolic trend, which increases along the direction of the black dotted arrow. From the obtained trend, two design schemes are picked (green and red) for further investigation as good thermoelectric generators and compared with the ARC-based proposal (blue). (b) Equilibrium flatband transmission function of all the cavity-based devices as a function of energy. The peaked transmission of the central RT region (without the ARC) is also shown here to emphasize the role of cavity engineering on transmission.

increase in h_{FP} from h. This finding closely matches with the theory presented above. Therefore, the design guideline to achieve boxcar transmission can be mathematically expressed as

$$\frac{|b_{\mathrm{FP}} - b/2|}{b/2} = \frac{1}{2}\frac{|h_{\mathrm{FP}} - h|}{h}. \tag{8}$$

The allowed design space of b_{FP} and h_{FP} is given by $b_{\min} \leq b_{\mathrm{FP}} \leq b/2$, $h \leq h_{\mathrm{FP}} \leq h_{\max}$, where $b_{\min}$ and $h_{\max}$ are the practical bounds of the cavity barrier width and height, respectively. In this case, based on the desired transmission goal, these bounds are set as $b_{\min} = b/4$ and $h_{\max} = 2h$.

It is also worth mentioning that within the allowed design space, the steady increase of Ω along the direction shown in Fig. 2(a) suggests that the boxcar nature can be further improved by utilizing another set of cavity designs. In order to justify this, we pick two sample design schemes of the FP cavity, namely, FP-II (green diamond) and FP-III (red star) as indicated in Fig. 2(a), alongside the typical ARC-based ($b_{\mathrm{FP}} = b/2$, $h_{\mathrm{FP}} = h$) proposal (FP-I, blue circle) [30,32]. Under flatband conditions, the equilibrium transmission functions of all the FP-based designs are plotted in Fig. 2(b) as a function of energy along with the standard RT transmission. The cavity design parameters corresponding to all the devices are presented in the legends of Fig. 2(b) in terms of the RT design parameters. We observe that, as compared to FP-I, the other schemes (FP-II and FP-III) tend to widen the transmission further preserving its desired shape and thereby improving Ω. One notable difference here is that the proposed designs (FP-II and FP-III) exhibit a slight dip in the transmission at energies below the resonating peak, unlike the ARC-based design. This might cause a slight reduction in the efficiency at lower values of the contact Fermi level. It is also important to note that the cavity region, based on its design, pulls the transmission minima to unity at a particular energy that might not always be the mid-band energy. In this case, Fig. 2(b) suggests that as the width of the cavity barrier is reduced, this energy tends to rise, which in turn widens the transmission bandwidth. Having obtained such transmission features, we strongly believe that the designs described here can be even better thermoelectric generators and hence should be investigated further.

III. DEVICE SCHEMATIC AND DESCRIPTION

Based on the design rules discussed in the last section, we depict the conduction-band schematics of all three cavity engineered devices (FP-I, FP-II, and FP-III), along with the standard resonant-tunneling device (RTD), in Figs. 3(b)–3(e). These devices have an ideal infinite extent in the transverse direction with a finite length along their transport direction (here, the z direction). The central RTD structure, as shown in Fig. 3(b), is modeled with a GaAs well of width $w = 4.2$ nm in between two $\mathrm{Al}_x\mathrm{Ga}_{1-x}\mathrm{As}$ barriers of width $b = 2.4$ nm each, where x is the aluminum mole fraction. Barrier height is kept fixed at 0.3 eV with respect to the well by precisely tuning the mole-fraction parameter. These design parameters are chosen in accordance with a realistic ground-state transmission full width at half maximum (FWHM) of $k_BT/2$, where k_B is the

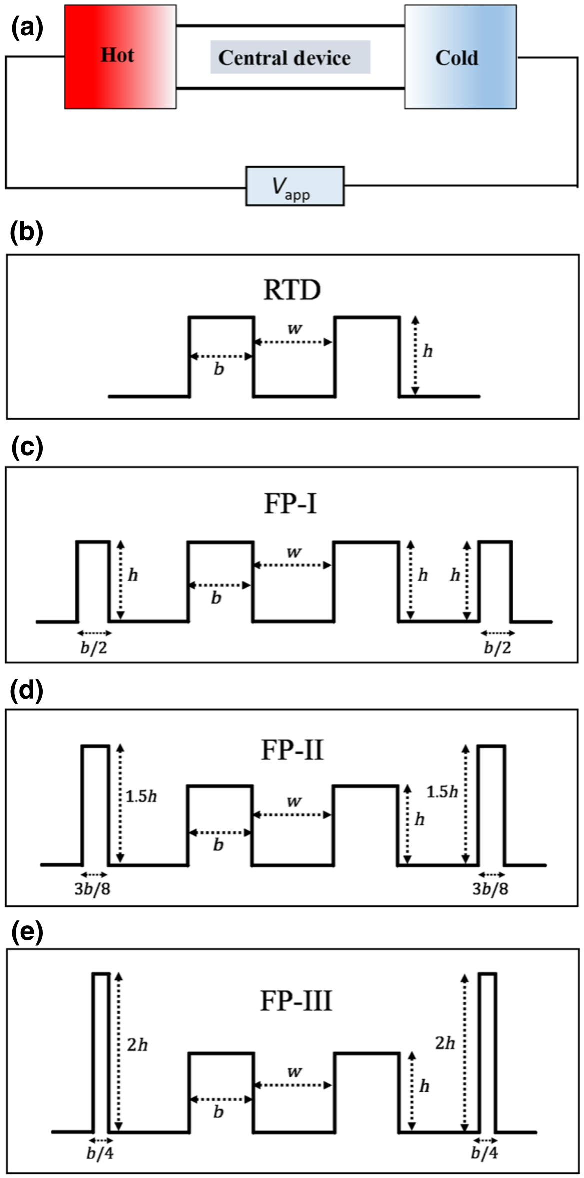

FIG. 3. Simulation setup and device schematics. (a) A typical voltage-controlled thermoelectric setup, where the central device is connected to two contacts of different temperatures externally joined by a load. The conduction-band schematics of four different TE device structures are depicted as follows. (b) RTD: a standard resonant-tunneling structure having the transmission FWHM equal to $k_BT/2$. This RTD device is embedded into three different FP cavity configurations, namely, (c) FP-I, $h_{\mathrm{FP}} = h$ and $b_{\mathrm{FP}} = b/2$; (d) FP-II, $h_{\mathrm{FP}} = 3h/2$ and $b_{\mathrm{FP}} = 3b/8$; and (e) FP-III, $h_{\mathrm{FP}} = 2h$ and $b_{\mathrm{FP}} = b/4$.

Boltzmann's constant and T denotes the temperature. For the cavity-based devices, the same RTD structure is symmetrically placed within the cavity regions such that the width of the well region between any two successive barriers remains the same at w. However, the varying design of the cavity wall gives rise to three differentstructures considered in this study, which are listed below:

(a) In Fig. 3(c), FP-I: $h_{\mathrm{FP}} = h$ and $b_{\mathrm{FP}} = b/2$.
(b) In Fig. 3(d), FP-II: $h_{\mathrm{FP}} = 3h/2$ and $b_{\mathrm{FP}} = 3b/8$.
(c) In Fig. 3(e), FP-III: $h_{\mathrm{FP}} = 2h$ and $b_{\mathrm{FP}} = b/4$.

The devices described above can be fairly accurately modeled using a nearest-neighbor tight-binding Hamiltonian of a linear atomic chain within the single-band effective mass approximation [38]. The GaAs/Al$_x$Ga$_{1-x}$As material system is chosen here because it has less variability of its effective mass over a wide range of compositions and excellent lattice-matching capability. Using the NEGF technique coupled with the charging effect, we present a comparative study of the devices discussed above in terms of the linear and nonlinear thermoelectric performance parameters. The device dimensions used here are in the order of the relaxation length scales, which eliminates the possibility of scattering to ensure a coherent transport of carriers within the ballistic limit [17]. On the other hand, the presence of nanostructured interfaces strongly restricts the flow of phonons in the device. This implies that the heat current flowing through the device is mainly due to electrons. Therefore, the lattice contribution to the thermal conductivity is ignored here.

The cavity-based devices manifest high immunity to the nonequilibrium changes in transmission function due to the charging effect. This results in improved trade-off characteristics for a wide range of contact Fermi levels. Furthermore, the widening of the transmission window allows a large number of additional transverse modes to conduct and contribute to the net charge current, which in turn boosts the power. Based on the results, we can definitely assert that the width of the transmission function obtained here is still below the ideal theoretical limit predicted by Whitney [24], which makes room for further research.

IV. SIMULATION METHODOLOGY AND SETUP

Figure 3(a) shows a typical voltage-controlled thermoelectric heat engine setup [39], which is used throughout for the purpose of simulation. The flow of electrons due to the thermal driving force from the hot to cold contact is opposed by the voltage drop across the load resistance connecting them. The polarity of this drop is such that it lowers the quasi-Fermi level of the hot contact with respect to the cold contact, which, as a result, causes an opposite flow of electrons. In the simulation framework, the variation of the load resistance is incorporated through the application of a positive voltage at the hot contact end.

The simulation methodology is mainly divided into two important parts, namely, (i) self-consistent estimation of the electronic transmission function and (ii) the calculation of charge and heat currents from the knowledge of the obtained transmission function. For the former part, we utilize the standard atomistic NEGF formalism [38,39] self-consistently coupled with the Poisson's equation. In order to analyze the device behavior under different operating conditions, we vary the equilibrium quasi-Fermi levels (E_f) of the hot (μ_H) and cold (μ_C) contacts. For a given applied bias of V_{app}, the Fermi level of the hot (cold) contact is shifted downward (upward) from its equilibrium value by an amount of $qV_{\mathrm{app}}/2$ due to symmetric electrostatic coupling, where q is the unit electronic charge. The simulation begins with a linear potential profile as an initial guess to calculate the longitudinal energy (E) resolved retarded Green's function $G(E)$, given by

$$G(E) = [(E + i0^+)\mathbb{I} - H - U(z) - \Sigma_H(E) - \Sigma_C(E)]^{-1}, \tag{9}$$

where $U(z)$ is the potential profile along the transport direction, $\Sigma_{H(C)}$ is the self-energy matrix of the hot (cold) contact, and $\mathbb{I}$ is the identity matrix. Having obtained $G(E)$, the carrier concentration (N) can be easily calculated from the electron correlation function, $G^n(E)$, which is then fed into the Poisson's equation to calculate the updated potential profile. The set of equations governing the above-mentioned routine are given by

$$G^n(E) = G[\Gamma_H f_{2D}(\mu_H) + \Gamma_C f_{2D}(\mu_C)]G^{\dagger}, \tag{10}$$

$$N = \frac{1}{\Delta z}\int \frac{G^n(E)}{2\pi} dE, \tag{11}$$

$$\frac{d^2}{dz^2}[U(z)] = \frac{-q^2}{\epsilon_0\epsilon_r}N, \tag{12}$$

where Δz is the discrete lattice spacing parameter; ϵ_0 is the free space permittivity; ϵ_r is the relative permittivity of GaAs, which is assumed to be uniform throughout the lattice; and $\Gamma_{H(C)}$ represents the broadening function of hot (cold) contact, which is defined as $\Gamma_{H(C)} = i\left[\Sigma_{H(C)} - \Sigma^{\dagger}_{H(C)}\right]$. The contributions from all the transverse modes are encapsulated in the f_{2D} function, which is defined as [38]

$$f_{2D}(E-\mu) = \frac{m_e^* k_B T}{2\pi\hbar^2}\log\left[1 + \exp\left(\frac{\mu - E}{k_B T}\right)\right], \tag{13}$$

where $\hbar$ is the reduced Planck's constant and m_e^* is the electron effective mass, which is considered to be uniform throughout the lattice. For our simulations, we take a constant effective mass of $0.07m_0$ across structures, where

m_0 is the free electron mass. The NEGF-Poisson simulation is performed self-consistently until the convergence is achieved and the nonequilibrium transmission function, $T(E)$, can thereby be calculated as

$$T(E) = \mathrm{Tr}[\Gamma_H G \Gamma_C G^\dagger]. \tag{14}$$

The resultant transmission function is then fed into the Landauer current formula to calculate the charge (J) and heat current (J^Q) densities [38]. Summing over all the current-carrying transverse modes and absorbing that in the f_{2D} function, the total charge current flowing through the device is given by

$$J = \frac{q}{\pi\hbar}\int dE T(E)[f_{2D}(E-\mu_H) - f_{2D}(E-\mu_C)]. \tag{15}$$

It is important to note that the total heat current, which is the energy-weighted particle current, is resolved into two components, namely, J_H^{Q1} and J_H^{Q2}, based on the contributions from longitudinal and transverse energy degrees of freedom, respectively. Therefore, the total heat current flowing through the hot contact (J_H^Q) is expressed as $J_H^Q = J_H^{Q1} + J_H^{Q2}$, where J_H^{Q1} and J_H^{Q2} are given by

$$J_H^{Q1} = \frac{1}{\pi\hbar}\int dE T(E)(E-\mu_H) \times [f_{2D}(E-\mu_H) - f_{2D}(E-\mu_C)], \tag{16}$$

$$J_H^{Q2} = \frac{1}{\pi\hbar}\int dE T(E)[g_{2D}(E-\mu_H) - g_{2D}(E-\mu_C)], \tag{17}$$

where the g_{2D} function is defined as [17,30]

$$g_{2D}(E-\mu) = \frac{m_e^\star}{2\pi\hbar^2}\int_0^\infty \frac{\epsilon_{\vec{k}_\perp} d\epsilon_{\vec{k}_\perp}}{1+\exp\left(\dfrac{E+\epsilon_{\vec{k}_\perp}-\mu}{k_B T}\right)}. \tag{18}$$

The integration in Eq. (18) is performed numerically where the upper limit of energy is chosen high enough to include all the significant transverse modes. We assume a parabolic dispersion relation ($\epsilon_{\vec{k}_\perp}$) in the transverse direction and the integration over all the momentum ($\vec{k}_\perp$) eigenstates is carried out with a periodic boundary condition.

Once the charge (J) and heat current (J_H^Q) densities are calculated, the output power density (P) and conversion efficiency (η) can be obtained using the standard thermoelectric setup [39] by the following relations:

$$P = JV_{\mathrm{app}}, \tag{19}$$

$$\eta = P/J_H^Q. \tag{20}$$

The efficiency is usually measured as a ratio to that of the Carnot's limit (η_C), defined as $\eta_C = 1 - T_C/T_H$, where $T_{H(C)}$ is the temperature of the hot (cold) contact. In the simulation, a steady temperature difference of 30 K is maintained between the contacts by setting $T_H = 330$ K and $T_C = 300$ K. The allowed range of power restricts the device operation between the short-circuit ($V_{\mathrm{app}} = 0$) and open-circuit ($V_{\mathrm{app}} = V_{\mathrm{OC}}$) condition, where V_{OC} is the open-circuit voltage.

V. RESULTS AND DISCUSSION

In this section, a detailed and comparative study of the results are discussed in terms of the nonlinear and linear response parameters. This study mainly focuses on the supremacy of the proposed device designs over the existing ones.

A. Nonlinear response analysis

1. Power and efficiency

In Fig. 4, output power per unit area of all the device structures is displayed as a function of V_{app} and contact E_f in a gray-scale color plot. It can be seen that the power starts to increase from the short-circuit condition with increasing V_{app} and reaches a local maxima before falling to zero at the onset of the open-circuit condition. Strictly speaking, net current actually reverses its direction at V_{OC} and, therefore, the setup cannot be used as a generator beyond this point. Usable power in the region beyond V_{OC} is thus treated as zero. This trend is almost similar irrespective of the design scheme, but what is important to

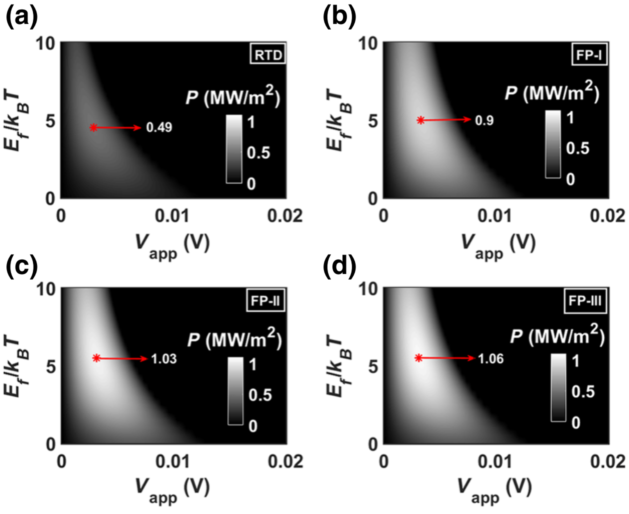

FIG. 4. Comparative study of output power: power density (in MW/m^2) of (a) RTD, (b) FP-I, (c) FP-II, and (d) FP-III devices as a function of the applied bias (V_{app}) and contact Fermi level (E_f). Enabling ARC (FP-I) over the RTD structure nearly doubles the generated output power for the entire range of E_f. The power can be further boosted between 15% and 18% by means of optimal cavity engineering as evident in the case of the design schemes FP-II and FP-III.

note here is the variation of power with E_f. When E_f is moved up in the energy scale from the lowest conduction-band edge, the net flow of electrons from the hot to cold contact increases steadily. This results in a monotonic rise of power until it reaches its peak value when the net electron flow becomes maximum. At this point, the overlap between the electronic density of states (DOS) and the region where $f_{2D}(\mu_H) - f_{2D}(\mu_C) > 0$, becomes maximum. This also indicates the most nonreversible state of the heat engine. With a further increase in E_f, power starts to die down steadily as the reverse flow (cold to hot) of electrons increases until E_f moves in the vicinity of the higher excited states. But, we restrict our study only within the contribution of the ground state as the excited states hardly contribute to the conduction due to their negligible electron population. Thus, the excited states are kept out of consideration. On the other hand, when E_f goes way down in energy, the power becomes negligible due to the lack of available states for conduction within the Fermi window. Therefore, we set the range of E_f between 0 and 10 k_BT in our simulation, where the reference energy $E = 0$ is chosen as the conduction-band minimum of GaAs.

Figure 4(a) displays the power density profile of the RTD-based TE device, which reveals that the maximum power of 0.49 $\mathrm{MW/m^2}$ can be delivered at $E_f = 4.5\ k_BT$. It is also important to observe that with increasing E_f, V_{OC} sharply falls due to the sharp nature of the transmission and, therefore, the power remains nonzero only for a narrow region of operation. On the other hand, the cavity-based devices, due to their band-pass nature of transmission, manifest a huge improvement in the power along with a broad spectrum as depicted in Figs. 4(b), 4(c), and 4(d) for the configurations FP-I, FP-II, and FP-III, respectively. Obtained results show that FP-II and FP-III designs can generate maximum power ($P_{\max}$) up to 1.03 $\mathrm{MW/m^2}$ and 1.06 $\mathrm{MW/m^2}$, respectively, as compared to 0.9 $\mathrm{MW/m^2}$ of the ARC-based proposal (FP-I) and 0.46 $\mathrm{MW/m^2}$ of the superlattice-based generators [27]. The position of $P_{\max}$ of FP-II and FP-III occurs at $E_f = 5.5\ k_BT$, which is slightly higher than that of FP-I, whose $P_{\max}$ occurs at $E_f = 5\ k_BT$. This result is in good agreement with the nature of the obtained transmission functions of the proposed designs as they are marginally shifted upward in energy when compared to that of FP-I. One must note that by deploying the proposed design schemes, $P_{\max}$ can be boosted up to a maximum of 18% and 116% over the ARC- and RTD-based proposal, respectively.

A device can only be qualified as a good heat engine if it can deliver a considerable amount of power at a high conversion efficiency. Therefore, an important parameter to judge here is the conversion efficiency, which dictates the ability of a generator to convert heat into electricity. Normalized conversion efficiencies (η/η_C) of all the devices are shown in Fig. 5 as a function of V_{app} and contact E_f. It is seen that the efficiency becomes maximum in the close vicinity of V_{OC} at $E_f = 0\ k_BT$ irrespective of the design scheme and decreases monotonically afterward with increasing E_f. However, theoretically, the efficiency can be improved further toward the ideal Carnot's limit at the cost of generated power by pushing E_f way down the conduction-band edge. But those devices would hardly be of any practical use due to their poor load-driving capability. Ideally, the heat current increases when the conduction takes place at higher energies. Therefore, the efficiency attains its maximum value when E_f is farthest below the ground transmission band. Within the mentioned simulation range, the highest efficiency that can be achieved in the RTD-based TE device is 61.5% at $E_f = 0\ k_BT$, as shown in Fig. 5(a). On the other hand, the cavity-based devices, although possessing wide transmission spectra, can offer even better efficiency due to their sharp transition profile of transmission, as evident from Figs. 5(b), 5(c), and 5(d) for FP-I, FP-II, and FP-III, respectively. The maximum attainable limit of efficiency that can be achieved through optimal cavity engineering is 64.4% for the aforementioned range of power, which is even better than 61.7% of the superlattice-based generators [27]. Obtained results clearly point toward improved power-efficiency trade-off characteristics, which are discussed next.

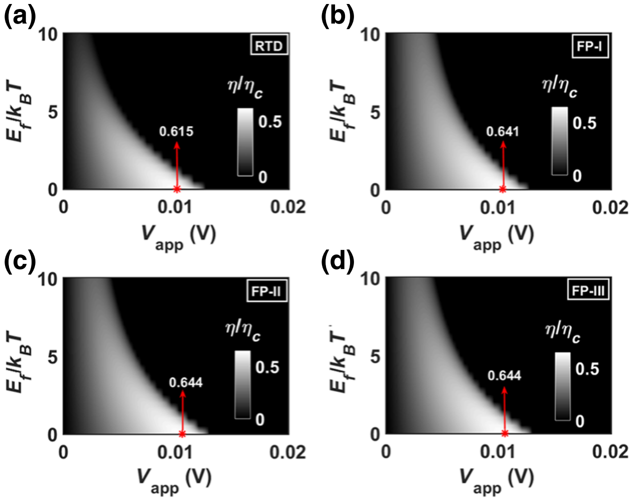

FIG. 5. Comparative study of efficiency: conversion efficiency normalized to Carnot's efficiency of (a) RTD, (b) FP-I, (c) FP-II, and (d) FP-III devices as a function of V_{app} and contact E_f. The efficiency in general becomes maximum in the close proximity of V_{OC} at $E_f = 0\ k_BT$. The cavity-based proposals show an almost similar range of efficiency, with a hint of improvement in the maximum value, as compared to the ARC-based device.

2. Power-efficiency product and trade-off

So far, we have quantitatively discussed the maximum achievable limit of the power and efficiency and their region of occurrence. We note that the variational trends followed by them are completely different in nature. But

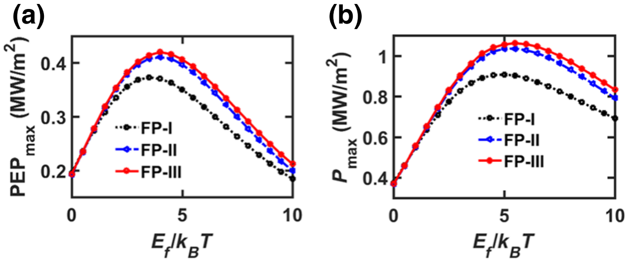

FIG. 6. Comparative analysis: (a) PEP$_{\max}$ and (b) $P_{\max}$ plotted with respect to different E_f for all the cavity engineered devices. The difference in the range of E_f pertaining to the maximum values of PEP$_{\max}$ and $P_{\max}$ directly points toward the trade-off between power and efficiency. It is also worth mentioning that as we move forward in the design order as in Fig. 2(a), we achieve even more improved power and PEP.

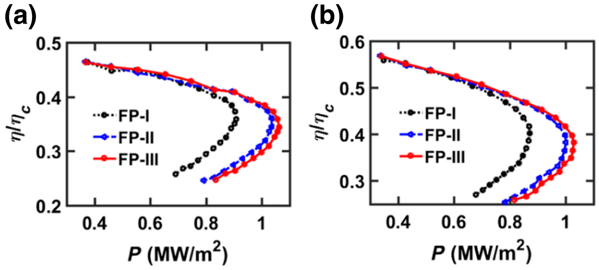

FIG. 7. Comparative analysis of power-efficiency trade-off along the locus of (a) $P_{\max}$ and (b) PEP$_{\max}$ for all of the cavity engineered devices. It is noted that, in both cases, the proposed design schemes enclose a larger area on the power-efficiency plane, which allows them to operate satisfactorily over a wide range of E_f.

to design an efficient heat engine, one must be extremely careful in choosing the regime of operation such that the device can deliver a significant amount of power at a high efficiency. In this context, instead of looking into the power and efficiency separately, their product (PEP) becomes more meaningful to inspect. For each value of E_f, the maximum of PEP (PEP$_{\max}$) with respect to the applied voltage is shown as a function of E_f in Fig. 6(a). We also plot the maximum power ($P_{\max}$) with respect to E_f in Fig. 6(b) in order to compare with PEP$_{\max}$. We notice that the maximum of PEP$_{\max}$ occurs around $E_f = 4\ k_BT$, well ahead of that of $P_{\max}$, which becomes maximum around $E_f = 5.5\ k_BT$. This clearly signifies that the efficiency falls rapidly with increasing E_f, which is also evident from the sharp fall of PEP$_{\max}$ beyond its maxima in contrast to $P_{\max}$. It is also worth mentioning that the margin of improvement in both parameters becomes maximum around their respective maxima, which further improves the trade-off.

Nonlinear studies of thermoelectric heat engines generally talk about the power-efficiency trade-off and the best operating regime of the device. Neither the power nor the efficiency is sufficient alone to judge the overall performance, as they are not mutually exclusive in nature. Therefore, we shift our attention toward determining the most suitable operating regime of these devices based on the specific design goals. A typical power-efficiency trade-off curve looks like a loop with the start (short-circuit condition) and end (open-circuit condition) points being the origin as shown in Fig. 3(a) in Ref. [30]. At any particular E_f, the loop is obtained by plotting the efficiency against power for all values of V_{app}. For any loop, one can always see that $P_{\max}$ and PEP$_{\max}$ occur at different values of V_{app}. Considering both aspects, we plot the trade-off boundaries along the locus of $P_{\max}$ and PEP$_{\max}$ for the series of loops at different values E_f in Figs. 7(a) and 7(b), respectively. The plots show that the trade-off characteristics improve significantly (enclosing a larger area) for the FP-II and FP-III structures as compared to the ARC-based (FP-I) device [30]. In this case, by improving we mean that the proposed devices can operate over a wide range of design parameters with satisfactory performance. A steady improvement in the trade-off begins to show up when E_f goes past 3 k_BT and maximizes in the range of $4 - 7\ k_BT$ for both cases. For a given range of efficiency between 30% and 40%, the respective power (in MW/m^2) corresponding to $P_{\max}$ and PEP$_{\max}$ varies between $0.8 - 0.9$ and $0.75 - 0.87$ for FP-I, $0.94 - 1.03$ and $0.9 - 1$ for FP-II, and $0.95 - 1.06$ and $0.94 - 1.03$ for FP-III. These results clearly indicate that the proposed devices offer excellent trade-off characteristics and perform significantly well within the suitable operating regime of E_f between 4 and 7 k_BT.

B. Linear response analysis

Using the same simulation framework, the linear response parameters can be extracted from the coupled charge and heat current equations, given by

$$I = G\Delta V + G_S\Delta T, \quad I_Q = G_P\Delta V + G_Q\Delta T, \tag{21}$$

where G, G_S, G_P, and G_Q are related to the corresponding Onsager coefficients [39]. ΔV and ΔT are the applied electrical and thermal bias, respectively, which are kept small enough to ensure linear operation.

1. Power factor and Seebeck coefficient

The power factor (σ) is defined as $\sigma = S^2G$, where G is the electrical conductivity and S is the Seebeck coefficient, which is given by $S = -G_S/G$. In Fig. 8(a), one can easily notice the sharp and steady rise of σ beyond $E_f = 2\ k_BT$ from FP-I to FP-III. The maximum improvement in σ that can be achieved through optimal cavity engineering over that of the ARC based design is nearly 20% in the range of E_f between 5 and 6 k_BT. This result actually points toward a monotonic improvement of G as the Seebeck coefficients of the cavity-based devices remain

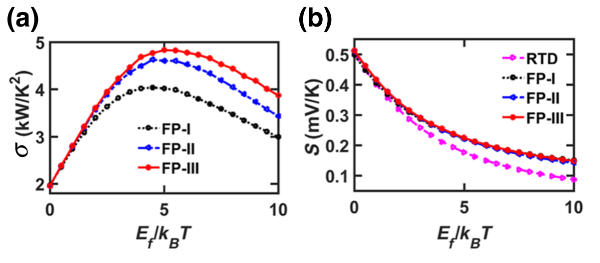

FIG. 8. Comparative analysis: (a) power factor (σ) and (b) Seebeck coefficient (S) plotted with respect to varying contact E_f. A steady improvement in σ is observed beyond $E_f = 2\ k_BT$ as we move up in the design order from FP-I to FP-III. The maximum improvement achieved in σ through cavity engineering is nearly 20% at E_f around $5-6\,k_BT$. On the other hand, there is no noticeable difference observed in S among the cavity engineered devices. However, when compared with the RTD-based TE device, they show serious improvement in S at higher values of E_f.

almost the same for the entire range of E_f, as depicted in Fig. 8(b). We understand that the marginal improvement in the transmission function does not affect V_{OC} much, but accounts for considerable gain in the σ due to the additional large number of transverse current-carrying modes that participate in conduction.

2. Figure of merit

Although the main goal of this work is to improve the nonlinear performance, it is customary to discuss the dimensionless figure of merit (zT) in order to judge the device's ability as an efficient heat engine. In our study, we restrict ourselves to the electronic part of heat conduction neglecting the phonon contribution. The presence of nanostructured interfaces strongly hinders the phonon transport through the lattice, which in turn results in a negligible thermal conductivity in contrast to its electronic counterpart. With these assumptions, zT can be expressed as

$$zT = \frac{\sigma}{G_{K,el}}T, \tag{22}$$

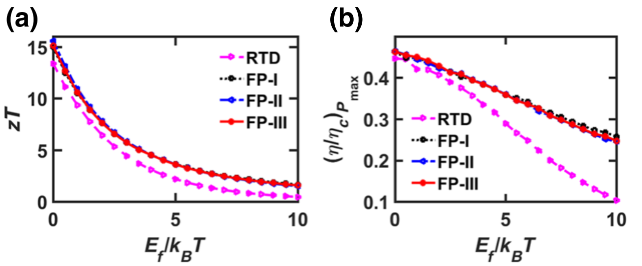

FIG. 9. Comparative analysis: (a) figure of merit (zT) and (b) efficiency at maximum power ($\eta_{P_{\max}}$) plotted for all the devices as a function of varying E_f. The cavity-based devices exhibit an almost similar zT and $\eta_{P_{\max}}$ for the entire range of E_f with a significant improvement over the RTD-based TE device. The range of zT and $\eta_{P_{\max}}$ of the cavity-based devices vary between $2.5-4.5$ and $31\%-39\%$, respectively, within the best operating regime of E_f between 4 and 7 k_BT.

where $G_{K,el}$ is the open-circuit electronic thermal conductivity, given by $G_{K,el} = G_Q - G_P G_S/G$. Figure 9(a) plots the zT of all the devices as a function of E_f, which clearly reveals that the boxcar feature of the transmission significantly enhances the zT throughout when compared to its peaked nature. This result is also in line with the variation of efficiency at maximum power ($\eta_{P_{\max}}$) with E_f as depicted in Fig. 9(b). It is observed that in the cavity-based devices, the achievable limit of zT and $\eta_{P_{\max}}$ within the suitable operating range of $E_f \simeq 4-7\,k_BT$ varies in between $2.5-4.5$ and $31\%-39\%$, respectively, which is fairly high as compared to $1.1-3.1$ and $20\%-34\%$ of a RTD-based TE device. These results show that at the respective maximum output power as shown in Fig. 4, the cavity-based generators can operate at up to 10% higher efficiency than that of a RTD-based TE device. One must also note that the range of zT is almost similar in all the cavity-based devices, which dictates that the heat-to-power conversion ability does not degrade with an associated rise in output power. A close look at the obtained result reveals that the steady improvement of σ from FP-I to FP-III is mostly suppressed by an equal rate of increase in the thermal conductivity, thereby maintaining a uniform zT. These results prove that the cavity engineered devices

TABLE I. Comparative study of key performance parameters.

Device configuration	RTD	FP-I	FP-II	FP-III
$P_{\max}$ (MW/m^2)	0.49	0.90	1.03	1.06
$\eta_{P_{\max}}$ (%)	44.66	46.34	46.42	46.32
$\eta_{\max}$ (%)	61.5	64.1	64.4	64.4
$\mathrm{PEP}_{\max}$ (MW/m^2)	0.18	0.37	0.41	0.42
$\sigma_{\max}$	2.20	4.03	4.62	4.82
$zT_{\max}$	13.37	14.98	15.57	15.09
$zT_{E_f\simeq 4-7\ k_BT}$	1.54–3.08	2.99–4.49	2.92–4.51	2.93–4.51
$S_{E_f\simeq 4-7\ k_BT}$ (mV/K)	0.15–0.21	0.2–0.25	0.2–0.25	0.2–0.26

perform much better in terms of an efficient heat engine as compared to RTD- [17] or QD-based [20] generators.

The results discussed above are quantitatively summarized in Table I for a detailed comparative study of all the devices. This study could also help in designing suitable TE heat engines according to the specific output goals.

VI. CONCLUSION

In conclusion, we explore the different design features of the electronic Fabry-Perot cavity over the RTD structure on achieving a nearly perfect band-pass electronic transmission. We show that there exist specific cavity design guidelines in such setups to achieve a boxcar-type transmission. Based on the obtained transmission profile, we pick two sample design proposals from the allowed design space with a foresight to achieve even better thermoelectric performance than the similar existing QD-, RTD-, ARC-, or superlattice-based proposals. Using the NEGF-Poisson formalism, we present a detailed and comparative study of the linear and nonlinear performance parameters in order to justify the superiority of the cavity engineered proposals. Obtained results reveal that by following the design guidelines, net deliverable power can be improved up to 18% from the ARC-based proposal at the same efficiency, leading to an excellent trade-off between them. It is also shown that by means of cavity engineering one can achieve a maximum of 116% more power at a 10% higher efficiency over the RTD-based heat engines. Also, in the linear response regime, the steady improvement of the power factor does not lead to a consequent degradation in the figure of merit and the Seebeck coefficient. Furthermore, we also discuss the suitable operating regime of these devices based on the margin of improvement and specific design criteria. We believe that our study opens up an avenue on designing transmission line-shape engineered solid-state devices for various applications with the simplest of structures that can be fabricated within the existing technological framework.

ACKNOWLEDGMENTS

The authors acknowledge funding from the Indian Space Research Organization as a part of the RESPOND grant. This work is an outcome of the research and development work undertaken in the project under the Visvesvaraya PhD Scheme of the Ministry of Electronics and Information Technology, Government of India, being implemented by Digital India Corporation (formerly Media Lab Asia).

[1] L. D. Hicks and M. S. Dresselhaus, Effect of quantum-well structures on the thermomagnetic figure of merit, Phys. Rev. B **47**, 727 (1993).

[2] L. D. Hicks and M. S. Dresselhaus, Thermoelectric figure of merit of a one-dimensional conductor, Phys. Rev. B **47**, 16631 (1993).

[3] L. D. Hicks, T. C. Harman, X. Sun, and M. S. Dresselhaus, Experimental study of the effect of quantum-well structures on the thermoelectric figure of merit, Phys. Rev. B **53**, R10493 (1996).

[4] G. D. Mahan and J. O. Sofo, The best thermoelectric, Proc. Natl. Acad. Sci. U.S.A. **93**, 7436 (1996).

[5] N. Nakpathomkun, H. Q. Xu, and H. Linke, Thermoelectric efficiency at maximum power in low-dimensional systems, Phys. Rev. B **82**, 235428 (2010).

[6] J. P. Heremans, M. S. Dresselhaus, L. E. Bell, and D. T. Morelli, When thermoelectrics reached the nanoscale, Nat. Nanotechnol. **8**, 471 (2013).

[7] A. Singha, S. D. Mahanti, and B. Muralidharan, Exploring packaging strategies of nano-embedded thermoelectric generators, AIP Adv. **5**, 107210 (2015).

[8] A. Majumdar, Thermoelectricity in semiconductor nanostructures, Science **303**, 777 (2004).

[9] G. J. Snyder and E. S. Toberer, Complex thermoelectric materials, Nat. Mater. **7**, 105 (2008).

[10] T. C. Harman, P. J. Taylor, M. P. Walsh, and B. E. LaForge, Quantum dot superlattice thermoelectric materials and devices, Science **297**, 2229 (2002).

[11] B. Poudel, Q. Hao, Y. Ma, Y. Lan, A. Minnich, B. Yu, X. Yan, D. Wang, A. Muto, D. Vashaee, X. Chen, J. Liu, M. S. Dresselhaus, G. Chen, and Z. Ren, High-thermoelectric performance of nanostructured bismuth antimony telluride bulk alloys, Science **320**, 634 (2008).

[12] J.-H. Bahk, Z. Bian, and A. Shakouri, Electron energy filtering by a nonplanar potential to enhance the thermoelectric power factor in bulk materials, Phys. Rev. B **87**, 075204 (2013).

[13] M. Thesberg, H. Kosina, and N. Neophytou, On the effectiveness of the thermoelectric energy filtering mechanism in low-dimensional superlattices and nano-composites, J. Appl. Phys. **120**, 234302 (2016).

[14] A. Singha and B. Muralidharan, Incoherent scattering can favorably influence energy filtering in nanostructured thermoelectrics, Sci. Rep. **7**, 7879 (2017).

[15] S. Hershfield, K. A. Muttalib, and B. J. Nartowt, Nonlinear thermoelectric transport: A class of nanodevices for high efficiency and large power output, Phys. Rev. B **88**, 085426 (2013).

[16] H. Karbaschi, J. Lovén, K. Courteaut, A. Wacker, and M. Leijnse, Nonlinear thermoelectric efficiency of superlattice-structured nanowires, Phys. Rev. B **94**, 115414 (2016).

[17] A. Agarwal and B. Muralidharan, Power and efficiency analysis of a realistic resonant tunneling diode thermoelectric, Appl. Phys. Lett. **105**, 013104 (2014).

[18] B. Sothmann, R. Sánchez, A. N. Jordan, and M. Büttiker, Powerful energy harvester based on resonant-tunneling quantum wells, New J. Phys. **15**, 095021 (2013).

[19] B. Sothmann, R. Sénchez, and A. N. Jordan, Thermoelectric energy harvesting with quantum dots, Nanotechnology **26**, 032001 (2015).

[20] B. Muralidharan and M. Grifoni, Performance analysis of an interacting quantum dot thermoelectric setup, Phys. Rev. B **85**, 155423 (2012).

[21] M. Esposito, K. Lindenberg, and C. Van den Broeck, Universality of Efficiency at Maximum Power, Phys. Rev. Lett. **102**, 130602 (2009).

[22] M. Esposito, R. Kawai, K. Lindenberg, and C. Van den Broeck, Efficiency at Maximum Power of Low-dissipation Carnot Engines, Phys. Rev. Lett. **105**, 150603 (2010).

[23] B. De and B. Muralidharan, Thermoelectric study of dissipative quantum-dot heat engines, Phys. Rev. B **94**, 165416 (2016).

[24] R. S. Whitney, Most Efficient Quantum Thermoelectric at Finite Power Output, Phys. Rev. Lett. **112**, 130601 (2014).

[25] R. S. Whitney, Finding the quantum thermoelectric with maximal efficiency and minimal entropy production at given power output, Phys. Rev. B **91**, 115425 (2015).

[26] C. H. Schiegg, M. Dzierzawa, and U. Eckern, Implementation of transmission functions for an optimized three-terminal quantum dot heat engine, J. Phys.: Condens. Matter **29**, 085303 (2017).

[27] P. Priyadarshi, A. Sharma, S. Mukherjee, and B. Muralidharan, Superlattice design for optimal thermoelectric generator performance, J. Phys. D: Appl. Phys. **51**, 185301 (2018).

[28] D. A. Broido and T. L. Reinecke, Effect of superlattice structure on the thermoelectric figure of merit, Phys. Rev. B **51**, 13797 (1995).

[29] H. H. Tung and C. P. Lee, An energy band-pass filter using superlattice structures, IEEE J. Quantum Electron. **32**, 507 (1996).

[30] S. Mukherjee, P. Priyadarshi, A. Sharma, and B. Muralidharan, Superior thermoelectric design via antireflection enabled lineshape engineering, IEEE Trans. Electron Devices **65**, 1896 (2018).

[31] C. Pacher, C. Rauch, G. Strasser, E. Gornik, F. Elsholz, A. Wacker, G. Kießlich, and E. Schöll, Antireflection coating for miniband transport and fabry-pérot resonances in gaas/algaas superlattices, Appl. Phys. Lett. **79**, 1486 (2001).

[32] S. Mukherjee and B. Muralidharan, Improved thermoelectric power efficiency trade-off via anti-reflection enabled resonant tunneling molecular wire, Integr. Ferroelectr. **194**, 37 (2019).

[33] J. Martorell, D. W. L. Sprung, and G. V. Morozov, Design of electron band pass filters for electrically biased finite superlattices, Phys. Rev. B **69**, 115309 (2004).

[34] G. V. Morozov, D. W. L. Sprung, and J. Martorell, Design of electron band-pass filters for semiconductor superlattices, J. Phys. D **335**, 3052 (2002).

[35] G. Bastard, Superlattice band structure in the envelope-function approximation, Phys. Rev. B **24**, 5693 (1981).

[36] Z. C. Zhao and D. R. McKenzie, Antireflection coating of barriers to enhance electron tunnelling: exploring the matter wave analogy of superluminal optical phase velocity, Sci. Rep. **7**, 12772 (2017).

[37] J. Stolle, C. Baum, R. Amann, R. Haman, T. Call, and W. Li, Coherent electron transparent tunneling through a single barrier within a fabry-perot cavity, Superlattices Microstruct. **95**, 140 (2016).

[38] S. Datta, *Quantum Transport: Atom to Transistor* (Cambridge University Press, Cambridge, 2005).

[39] S. Datta, *Lessons from Nanoelectronics: A New Perspective on Transport*, Lecture Notes Series (World Scientific Publishing Company, 2012).